Supporting Information

Highly efficient and selective nitrate electroreduction to ammonia catalyzed by molecular copper catalyst@Ti$_3$C$_2$T$_x$ MXene

Lan-Xin Li,[a] Wu-Ji Sun, [a] Hao-Yu Zhang, [a] Jia-liang Wei, [a] Shu-Xian Wang, [a] Jing-Hui He, * [a] Na-Jun Li, [a] Qing-Feng Xu, [a] Dong-Yun Chen, [a] Hua Li, [a] Jian-Mei Lu* [a]

E-mail: jinghhe@suda.edu.cn; lujm@suda.edu.cn

1. Experimental Procedures and methods

1.1 Pre-treatment of carbon cloth

The hydrophilic surface of carbon cloth was treated with oxygen plasma for 5min, and the hydrophobic surface was treated for 15min. After the hydrophilic treatment, carbon cloth was treated with acetone, ethanol and ultra-pure water ultrasound for 20min, and then dried for use.

1.2 Determination of ion concentration.

The concentration of ions in the electrolyte before and after dilution was measured with the ultraviolet-visible (UV-Vis) spectrophotometer to match the range of the calibration curve. Specific detection methods are as follows:

(1) Detection of nitrate-N concentration：

First, 0.1 mL of 1 M HCl and 0.01 mL 0.8 wt% sulfamic acid solution was added into the diluted highly concentrated electrolytes with stirring. Then, the solution was allowed to stand for 15 min. A standard curve was used to accurately determine the concentration of nitrate-N in the electrolyte from the value of A generated by an UV-Vis spectrophotometer (λ= 220 nm and 275 nm), which was calculated as $A=A_{220nm}-2*A_{275nm}$. The standard curve was obtained by a series of different nitrate-N concentration-absorbance curves prepared with potassium nitrate.

(2) Detection of nitrite-N concentration：

4 g of p-aminobenzenesulfonamide and 0.2 g of N-(1-Naphthyl) ethylenediamine dihydrochloride were dissolved in 10 mL of phosphoric acid. After stirring, it waspoured into 50 mL of ultrapure water to obtain Griess reagent. 0.1 mL of Griess reagent was added into the electrolyte which was diluted to the appropriate concentration range, then being shaked and let stand for 15 minutes, and its absorption value at 540 nm was measured and recorded by an UV-Vis spectrophotomete. The absorbance was substituted by the standard curve to calculate the nitrite-N concentration. The standard curve was obtained by a series of different nitrate-N concentration-absorbance curves prepared with sodium nitrite.

(3) Detection of ammonia-N concentration：

The ammonia-N concentration is determined by Nessler's reagent method. 0.1 mL of 500 g/L potassium sodium tartrate masking agent was added into the electrolyte which was diluted to a suitable concentration range, and 0.1 mL Nessler's reagent was added after being shake well. The absorbance at 420 nm was measured and recorded by an UV-Vis spectrophotometer after standing for 20 minutes. Then the absorbance was substituted by the standard curve to calculate the ammonia-N concentration. The standard curve was obtained by a series of different ammonia-N concentration-absorbance curves prepared with ammonium sulfate.

1.4 ^{15}N Isotope Labeling Experiments

Using $^{15}NaNO_3$ (>99.0%) as nitrogen source to carry out nitrate reduction isotope labeling experiments. 0.5 M Na_2SO_4 was used as electrolyte, and 50 mg/L of $^{15}NO_3^--N$

was added to the cathode compartment as reactant. After electrolysis, the pH of 50

mL of the cathodic reaction solution was adjusted to about 4-5 with 4 M H_2SO_4, and

maleic acid was used as an external standard for quantification by ^1H NMR. The

calibration curve was created as follows: Firstly, a series of $^{15}NH_4^+$-^{15}N (($^{15}NH_4)_2SO_4$)

solutions with known concentration (10, 20, 30, 40, 50 mg/L) were prepared in 0.5M

Na_2SO_4. Secondly, 1 mL of 20 g/L maleic acid solution was added into 50mL of the

$^{15}NH_4^+$-^{15}N standard solution. Thirdly, 50 μL of D_2O was added into 500 μL of the above

solution for the ^1H NMR detection. Fourthly, since the concentration of $^{15}NH_4^+$-^{15}N was

positively correlated with the area ratio, the peak area ratio of $^{15}NH_4^+$-^{15}N and maleic

acid were used for calibration. Similarly, $Na^{14}NO_3$ was used as the nitrogen source of

$^{14}NO_3^-$-^{14}N, and the calibration curve was created with $(NH_4)_2SO_4$.

1.5 Online differential electrochemical mass spectrometry (DEMS) tests

Online DEMS (QAS 100) was measured by Linglu instruments (Shanghai) Co. Ltd was

used to detect the intermediates during the reaction. 0.1 M Na_2SO_4 with 1000 ppm

$NaNO_3$-N was used as electrolyte. The counter electrode and reference electrode were

a Pt foil and a SCE electrode, respectively. CuPc@MXene powder was dispersed in

ethanol to form a catalyst ink, and then the ink was dropped on the gold foil. Dried

gold foil acted as the working electrode. The Ar (99.99 % purity) was introduced to

remove the gas impurities in the electrolyte for 30 min before the test. The differential

mass signals were obtained during the electrochemical LSV process employed from -

0.5 to -2 V vs. SCE at a scan rate of 5 mV s^{-1} after the baseline kept steady. In order to

reduce the error of the experiment, four cycles of experiment were carried out.

1.6. Theoretical simulation

All the Density functional theory calculations were performed by using the Vienna Ab-initio Simulation Package (VASP) with the Projected Augmented Wave method[1, 2]. The exchange-correlation interactions were described by the generalised gradient approximation (GGA) [3] in the form of the Perdew-Burke-Ernzerhof functional (PBE) [4]. For all the geometry optimizations, the cut-off energy was set to 500 eV and the convergence threshold was 10^{-5} eV, and 5×10^{-3} eV/Å for energy and force, respectively. The weak interaction was described by DFT+D3 method using empirical correction in Grimme's scheme [5]. At least 20 Å vacuum space was applied in the z-direction of the slab models, preventing the vertical interaction between slabs. The reaction Gibbs free energy changes (ΔG) for each elementary steps were based on the computational hydrogen electrode model, which can be calculated by the following equation:

$$\Delta G = \Delta E + \Delta ZPE - T\Delta S$$

where ΔE is obtained directly from DFT calculations, ΔZPE is the change of zero-point energies (ZPE), T is the temperature of 298.15K, and ΔS is the change in entropy.
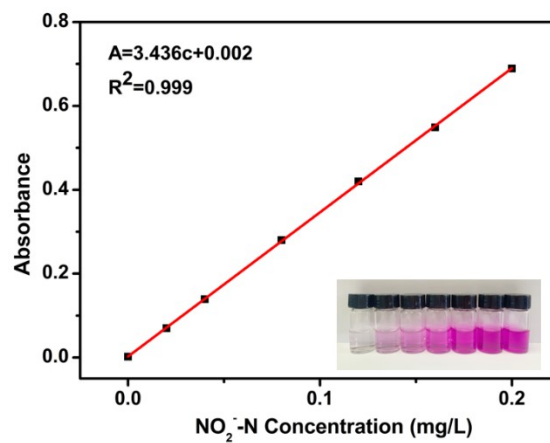
1.7. Voltage conversion

For all the electrochemical tests performed, the applied potentials were converted to the reversible hydrogen electrode (RHE) scale through the following equation:

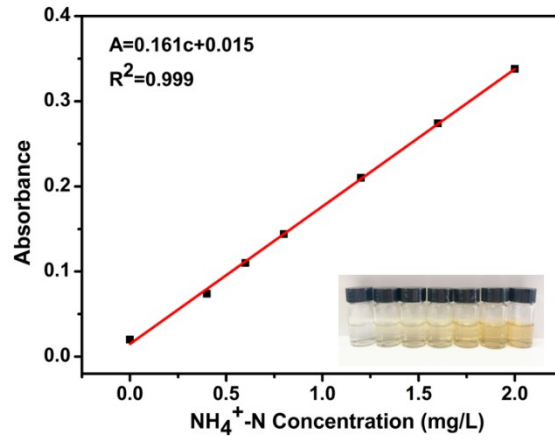$$E_{RHE} = E_{SCE} + 0.0591 \times pH + 0.242$$
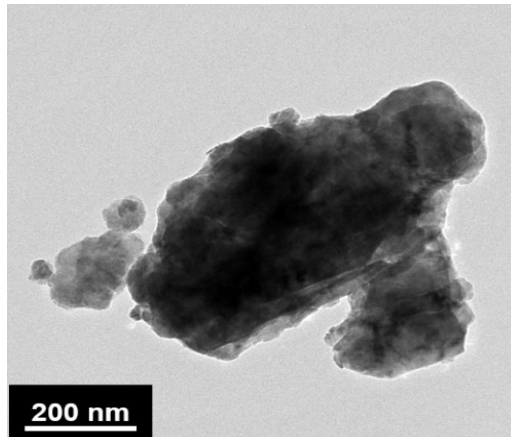
2. Supplementary figures and tables
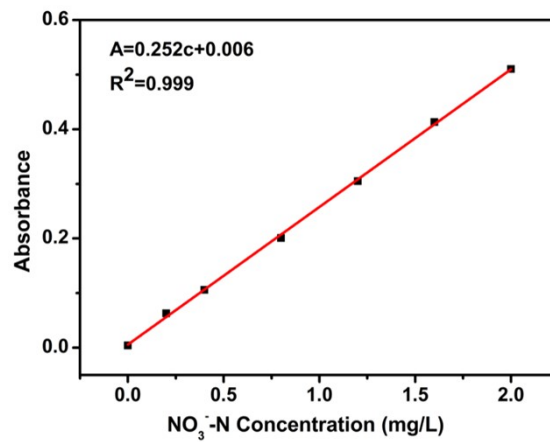
Figure S1 The concentration-absorbance calibration curves of nitrate-N with good
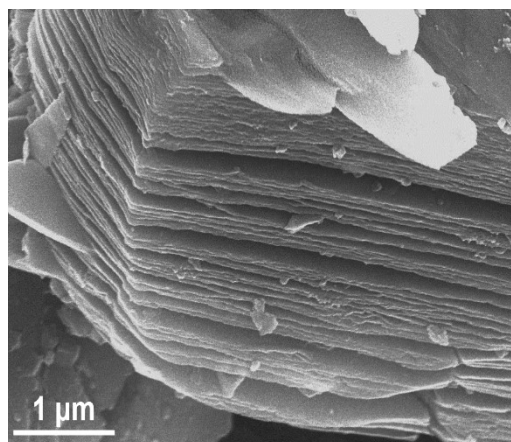
linearity.

Figure S2 The concentration-absorbance calibration curves of nitrite-N with good

linearity.

Figure S3 The concentration-absorbance calibration curves of ammonia-N with good linearity.

Figure S4 TEM images of Ti_3AlC_2 MAX

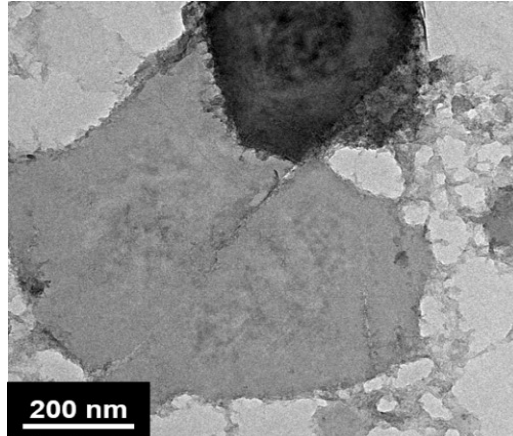**Figure S5** SEM images of $Ti_3C_2T_x$ after etching Ti_3AlC_2

Figure S6 TEM images of stacked $Ti_3C_2T_x$
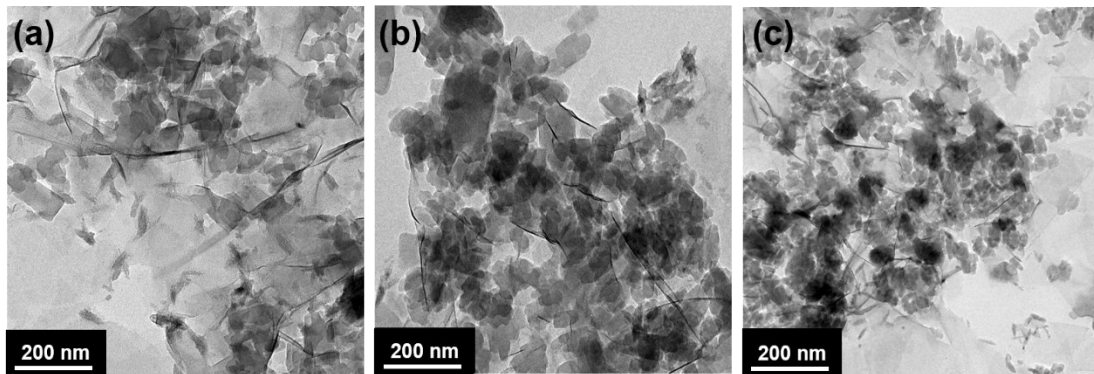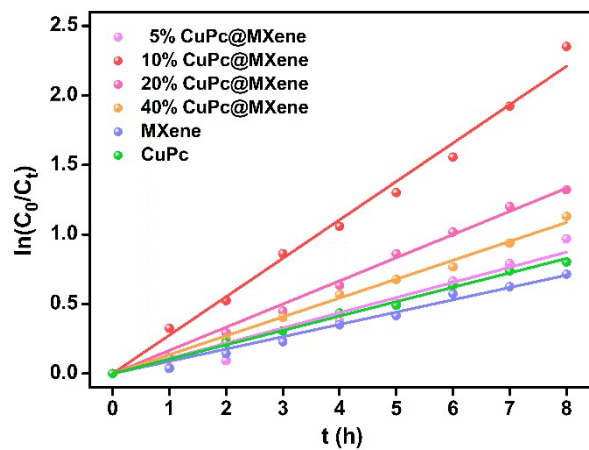

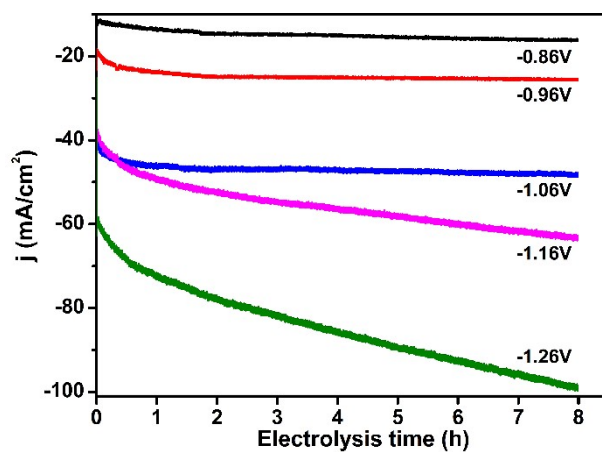**Figure S7** TEM images of (a) 5 %, (b) 20 % and (c) 40% CuPc@MXene.
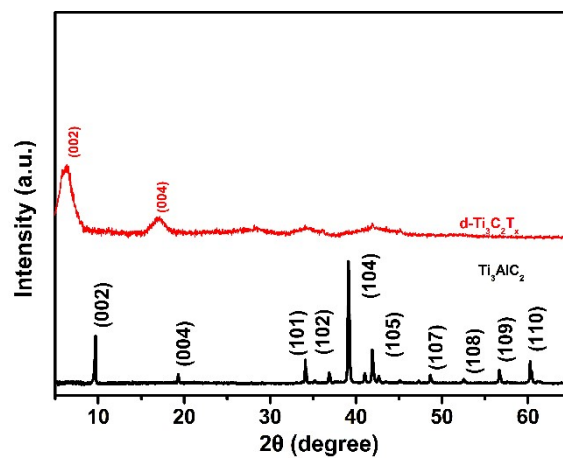
Figure S8 XRD patterns of d-$Ti_3C_2T_x$ and Ti_3AlC_2

Figure S9 First-order kinetic analysis for the data of plots

Figure S10 The i-t curves of 10% CuPc@MXene under different application voltages

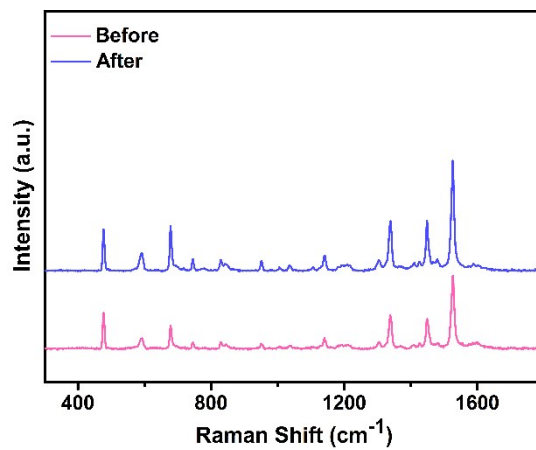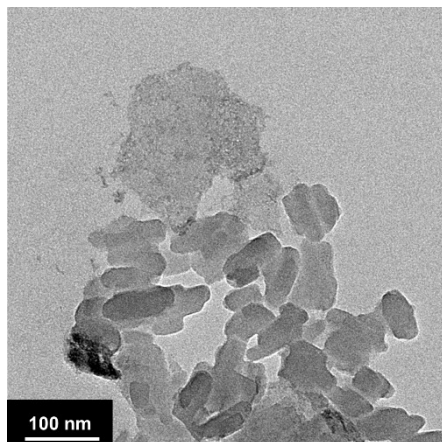**Figure S11** Raman spectra of 10% CuPc@MXene before and after stability test.

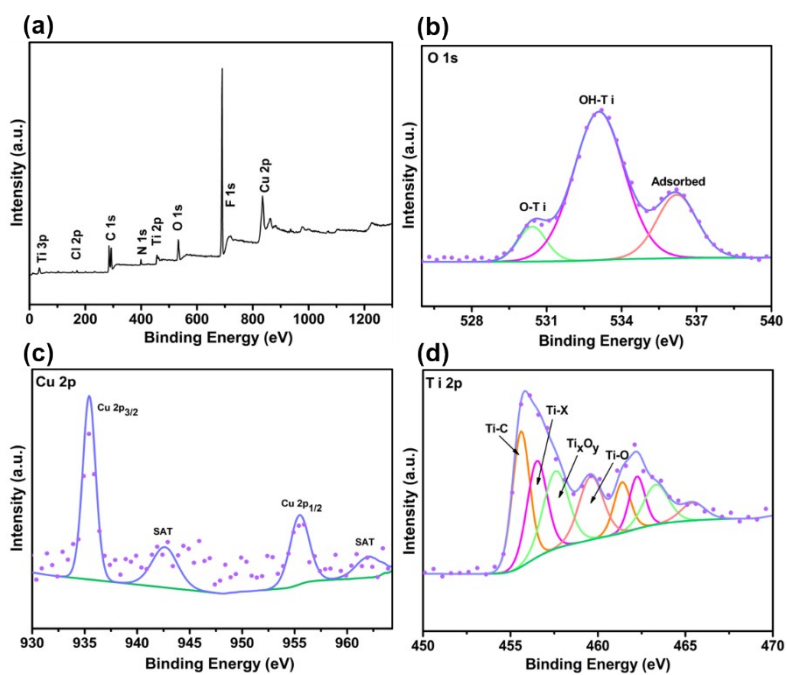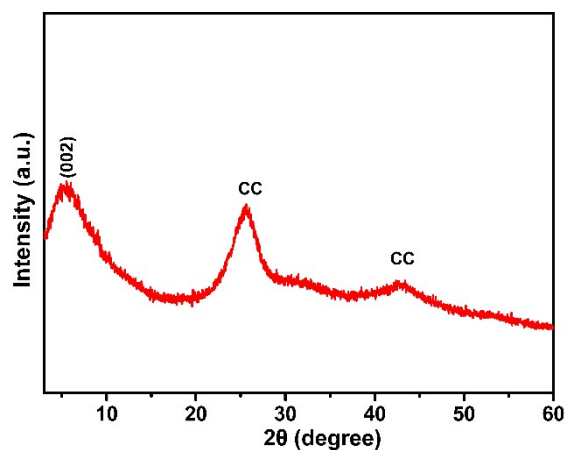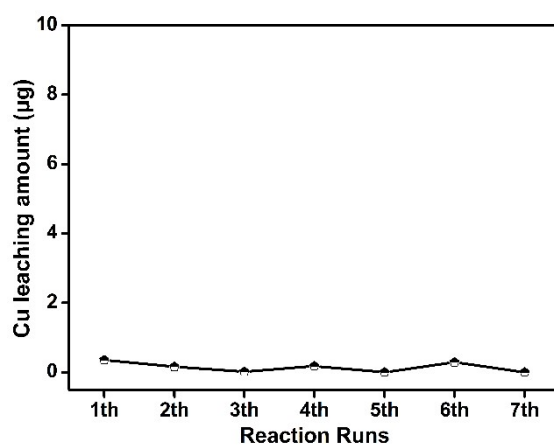**Figure S12 TEM imagin of 10% CuPc@MXene after stability test.**

Figure S13 XPS spectra of CuPc@MXene after stability test: (a) total survey, (b) O
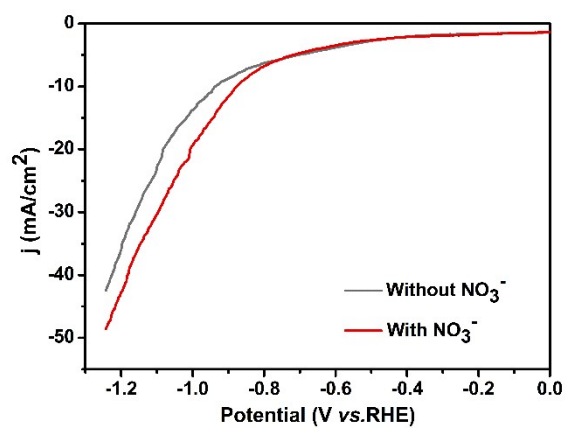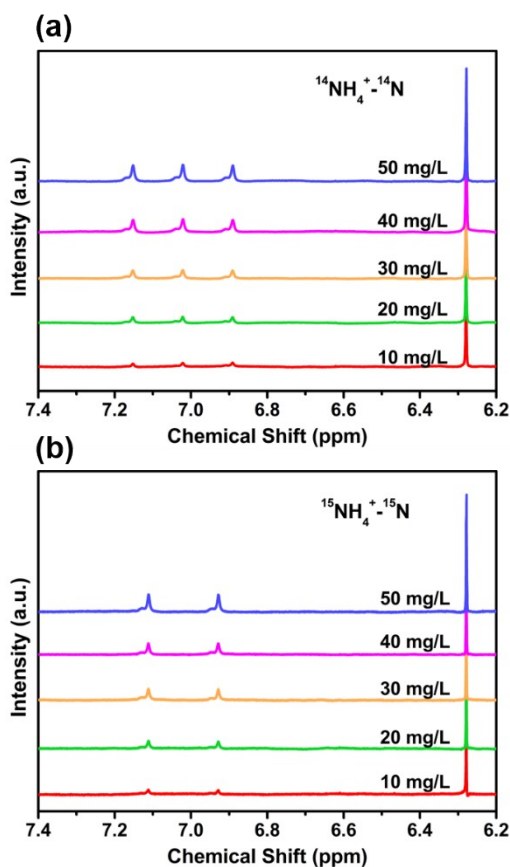
1s, (c) Cu 2p, (d) Ti 2p

Figure S14 XRD patterns of CuPc@MXene after stability test. (Carbon cloth loaded with catalysts was directly tested by XRD, and CC denotes the characteristic peak of carbon cloth)
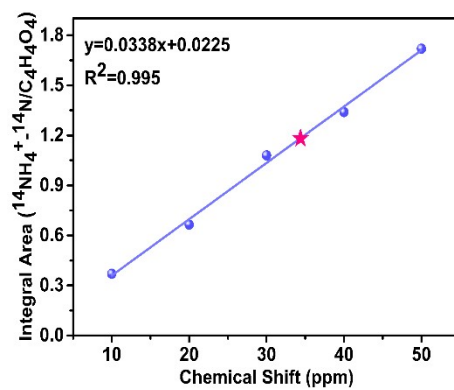

Figure S15 Cu leaching amount of the 10% CuPc@MXene during stability tests.
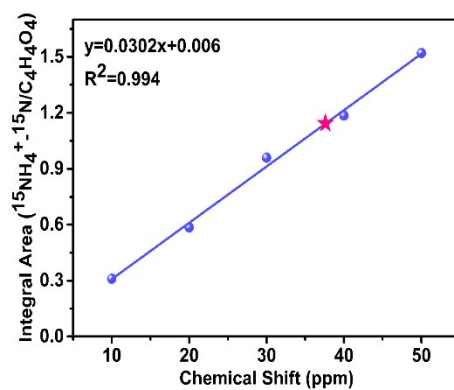
Figure S16 LSV curves of 10% CuPc@MXene in 0.5M Na$_2$SO$_4$ electrolyte with and without NO$_3^-$.

Figure S17 The ^{1}H NMR spectra of (a) ^{14}NH$_4^+$-^{14}N and (b). ^{15}NH$_4^+$-^{15}N with different concentrations. Since the nuclear magnetic resonance peak area is directly related to the ammonium content, ^{1}H NMR can be used to quantitatively determine the concentration of NH$_4$$^+$-N with external standards (maleic acid). The proton signal of maleic acid appears at δ= 6.27 ppm. The ^{1}H NMR spectrum of ^{15}NH$_4^+$ has double peaks at δ= 7.11 and 6.93 ppm, while ^{14}NH$_4^+$ has three peaks at δ = 7.15, 7.02 and 6.89 ppm.

Figure S18 The calibration curve of integral area ($^{14}NH_4^+$-$^{14}N/C_4H_4O_4$) against $^{14}NH_4^+$-^{14}N concentration.

Figure S19 The calibration curve of integral area ($^{15}NH_4^+$-$^{15}N/C_4H_4O_4$) against $^{15}NH_4^+$-^{15}N concentration.

Figure S20 CV curves of (a) CuPc, (b) MXene and (c) 10% CuPc@MXene with scan rates from 20 to 160 mV s^{-1}. (d) Plots of the current density versus the scan rate for 10% CuPc@MXene, CuPc and MXene. The specific capacitance for a flat surface is generally found to be in the range of 20-60 μF cm^{-2}. In the following calculations of electrochemical active surface area we assume 40 μF cm^{-2}. The measured capacitive currents are plotted as a function of scan rate in **Figure S20d** and a linear fit determined the specific capacitance to be 32.68 mF cm^{-2} for 10% CuPc@MXene, 12.93 mF cm^{-2} for CuPc, 16.30 mF cm^{-2} for MXene.

$$A_{ECSA}^{CuPc@MXene} = \frac{32.68 mF\ cm^{-2}}{40 \mu F\ cm^{-2}} = 817.00 cm^2_{ECSA}$$

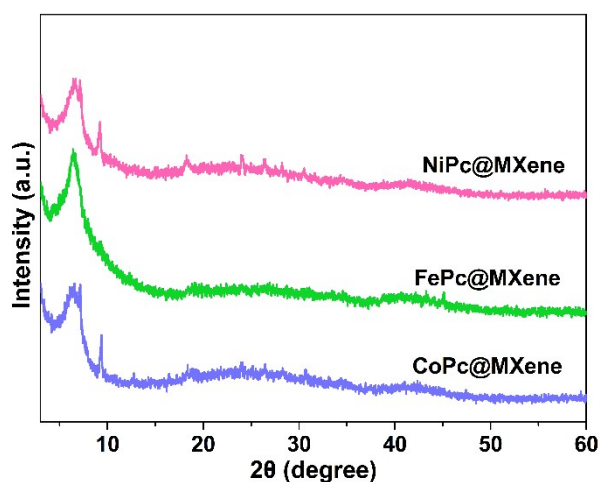$$A_{ECSA}^{CuPc} = \frac{12.93 mF\ cm^{-2}}{40 \mu F\ cm^{-2}} = 323.25 cm^2_{ECSA}$$

$$A_{ECSA}^{MXene} = \frac{16.30 mF\ cm^{-2}}{40 \mu F\ cm^{-2}} = 407.50 cm^2{}_{ECSA}$$
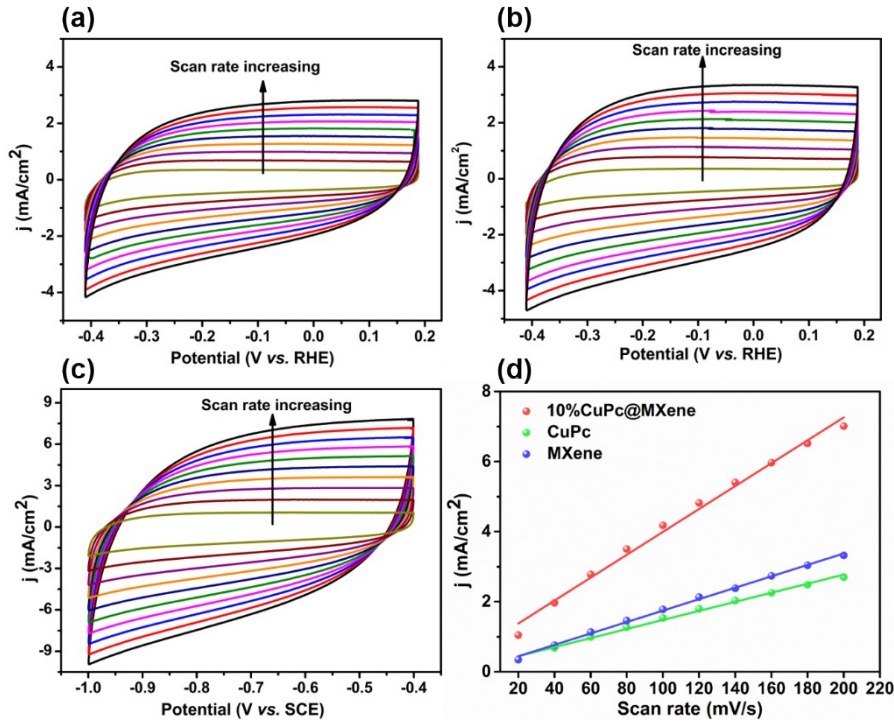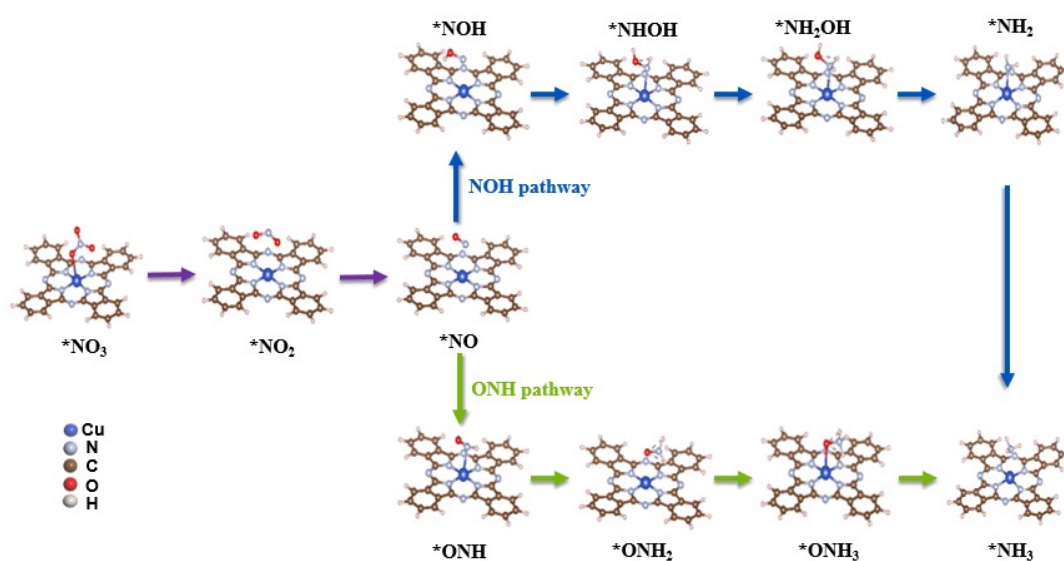
Figure S21 Structural models and reaction pathway of NO_3^- electroreduction on CuPc@MXene.
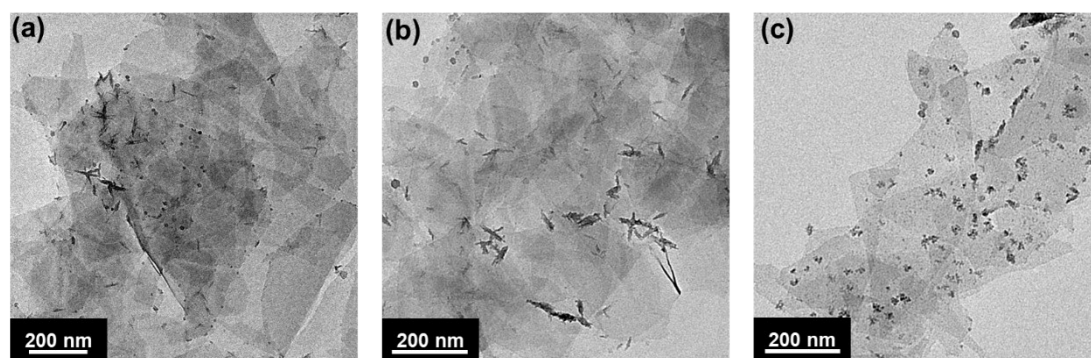
Figure S22 TEM image of (a) NiPc@MXene, (b) FePc@MXene, (c) CoPc@MXene.

Figure S23 XRD patterns of NiPc@MXene, FePc@MXene and CoPc@MXene.

Table S1. Comparison of electroredution performance over CuPc@MXene with other reported electrocatalysts.

Elecrocatalyst	Electrolyte	performance	Ref.
CuPc@Mxene	50 mg/L NO_3^--N 0.5 M Na_2SO_4	R_{NH3} = 78.9% S_{NH3} = 94.0% Y_{NH3} = 0.72 mg/(h^{-1}·cm^{-2})	This work
Ag-Ni films	20 mM $NaNO_3$	R_{NH3} = 56% S_{NH3} = 80.4%	6
Cu–PTCDA	500 ppm NO_3^--N 0.1 M phosphate buffer	S_{NH3} = 27% Y_{NH3} = 0.436 mg/(h^{-1}·cm^{-2})	7

TiO$_2$ nanotubes/ TiO$_{2-x}$	50 ppm NO$_3^-$-N 0.5 M Na$_2$SO$_4$	S$_{NH3}$=87.1%	8
Cu Nanobelt	30 ppm NO$_3^-$-N 0.05 M Na$_2$SO$_4$	S$_{NH3}$=90.0%	9
Co/CoO NSAs	200 ppm NO$_3^-$-N 0.1 M Na$_2$SO$_4$	S$_{NH3}$=91.2%	10
Co$_3$O$_4$-TiO$_2$/Ti	50 ppm NO$_3^-$-N, 0.1 M Na$_2$SO$_4$	S$_{NH3}$=77% Y$_{NH3}$=0.137 mg/(h^{-1}·cm^{-2})	11
PPy–Cu	50 mM KNO$_3$ 0.1 M LiClO$_4$	R$_{NH3}$=33.6%	12
Cu$_{80}$Ni$_{20}$	20 mM NaNO$_3$ 1 M NaOH	R$_{NH3}$=50%	13
Ni-TiO$_2$ nanotube array	50 mg/L NO$_3^-$-N 0.5 g/L Na$_2$SO$_4$	S$_{NH3}$=53.53% Y$_{NH3}$=0.067 mg/(h^{-1}·cm^{-2})	14
Cu Modified Pt Nanoflowers	280mg/L NO$_3^-$-N 0.1M NaOH	R$_{NH3}$=22.50% S$_{NH3}$=25.4%	15
Cu–Pt	0.05 M KNO$_3$	S$_{NH3}$=36% Y$_{NH3}$=0.272 mg/(h^{-1}·cm^{-2})	16
Fe	100mg/L N-NO$_3^-$ 500 mg/L Na$_2$SO$_4$	S$_{NH3}$=52.1% Y$_{NH3}$=0.15 mg/(h^{-1}·cm^{-2})	17

copper rotating cylinder	30 mM KNO$_3$ 0.1 M K$_2$SO$_4$	S$_{NH3}$=86%	18
Cu/Cu$_2$O NWAs	200 ppm NO$_3^-$-N 0.5 M Na$_2$SO$_4$	S$_{NH3}$=81.2%	19
Pt–Cu	0.02 M KNO$_3$	S$_{NH3}$=45% Y$_{NH3}$=0.136 mg/(h^{-1}·cm^{-2})	20

Table S2. Theoretical and measured Cu and Ti molar ratio of catalysts with different

Theoretical molar ratio (%)	Actual molar ratio (%)
5	7.78
10	10.71
20	23.67
40	38.80

molar ratios.

Table S3

Quantitative Method	Nitrogen sources	Concentration of $^{14}NH_4^+$-^{14}N / $^{15}NH_4^+$-^{15}N (mg/L)	NH$_3$ yield rate (mg·h^{-1}·cm^{-2})
Colorimetric method	$^{14}NO_3^-$	35.56	0.54
^{1}H NMR	$^{14}NO_3^-$	34.25	0.52

^{1}H NMR	**$^{15}NO_3^-$**	**37.72**	**0.57**

Table S4

	Selectivity for ammonia (%)	Conversion (%)	NH$_3$ yield rate (mg·h^{-1}·cm^{-2})
FePc@MXene	64.1	79.2	0.33
CoPc@MXene	42.5	71.1	0.18
NiPc@MXene	61.7	77.6	0.30
CuPc@MXene	85.7	90.5	0.67

References

1. G. Kresse and J. Furthmüller, *Physical Review B*, 1996, **54**, 11169-11186.
2. G. Kresse and J. Furthmüller, *Computational Materials Science*, 1996, **6**, 15-50.
3. J. P. Perdew, K. Burke and M. Ernzerhof, *Phys. Rev. Lett.*, 1996, **77**, 3865-3868.
4. J. P. Perdew, M. Ernzerhof and K. Burke, *The Journal of Chemical Physics*, 1996, **105**, 9982-9985.
5. S. Grimme, *J. Comput. Chem.*, 2006, **27**, 1787-1799.
6. L. Mattarozzi, S. Cattarin, N. Comisso, N. El Habra, P. Guerriero, M. Musiani and L. Vázquez-Gómez, *Electrochim. Acta*, 2020, **346**, 136240.
7. G.-F. Chen, Y. Yuan, H. Jiang, S.-Y. Ren, L.-X. Ding, L. Ma, T. Wu, J. Lu and H. Wang, *Nat. Energy*, 2020, **5**, 605-613.
8. R. Jia, Y. Wang, C. Wang, Y. Ling, Y. Yu and B. Zhang, *ACS Catal.*, 2020, **10**, 3533-3540.
9. X. Wang, M. Zhu, G. Zeng, X. Liu, C. Fang and C. Li, *Nanoscale*, 2020, **12**, 9385-9391.
10. Y. Yu, C. Wang, Y. Yu, Y. Wang and B. Zhang, *Science China Chemistry*, 2020, **63**, 1469-1476.
11. J. Gao, B. Jiang, C. Ni, Y. Qi, Y. Zhang, N. Oturan and M. A. Oturan, *Appl. Catal. B Environ.*, 2019, **254**, 391-402.
12. D. Çirmi, R. Aydın and F. Köleli, *J. Electroanal. Chem.*, 2015, **736**, 101-106.
13. L. Mattarozzi, S. Cattarin, N. Comisso, P. Guerriero, M. Musiani, L. Vázquez-Gómez and E. Verlato, *Electrochim. Acta*, 2013, **89**, 488-496.

14.   F. Liu, K. Liu, M. Li, S. Hu, J. Li, X. Lei and X. Liu, *Chemosphere*, 2019, **223**, 560-568.

15.   T. Chen, Y. Li, L. Li, Y. Zhao, S. Shi, R. Jiang and H. Ma, *Catalysts*, 2019, **9**.

16.   M. A. Hasnat, S. Ben Aoun, S. M. Nizam Uddin, M. M. Alam, P. P. Koay, S. Amertharaj, M. A. Rashed, M. M. Rahman and N. Mohamed, *Applied Catalysis A: General*, 2014, **478**, 259-266.

17.   M. Li, C. Feng, Z. Zhang, S. Yang and N. Sugiura, *Bioresour. Technol.*, 2010, **101**, 6553-6557.

18.   O. González Pérez and J. M. Bisang, *Electrochim. Acta*, 2016, **194**, 448-453.

19.   Y. Wang, W. Zhou, R. Jia, Y. Yu and B. Zhang, *Angew. Chem. Int. Ed.*, 2020, **59**, 5350-5354.

20.   M. A. Hasnat, M. A. Rashed, S. Ben Aoun, S. M. N. Uddin, M. Saiful Alam, S. Amertharaj, R. K. Majumder and N. Mohamed, *J. Mol. Catal. A: Chem.*, 2014, **383-384**, 243-248.